Distribution of plastics of various sizes and densities in the global ocean from a 3D Eulerian model

Zih-En Tseng[1], Yue Wu[1], Dimitris Menemenlis[2], Guangyao Wang[1], Chris Ruf[3], Yulin Pan[1]

[1]Naval Architecture and Marine Engineering, the University of Michigan, MI, United States
[2]Jet Propulsion Laboratory, California Institute of Technology, CA, United States
[3]Climate and Space Sciences and Engineering, the University of Michigan, MI, United States

Key Points:

- We develop a 3D Eulerian model to study the transport of microplastics in the global ocean, taking into consideration the effect of size and density of particles to their vertical terminal velocity.
- Stationary patterns from particles of different properties are studied, among which only low-density particles with sufficient size ($\gtrsim 10\mu m$) accumulate in subtropical gyres observed in previous studies.
- Seasonal variation of the surface particle concentration is demonstrated, which reasonably agrees with satellite observation by CYGNSS and is physically attributed to the seasonal variation of ocean mixing layer (ML) depth.

Corresponding author: Yulin Pan, `yulinpan@umich.edu`

Abstract

We develop a 3D Eulerian model to study the transport and distribution of microplastics in the global ocean. Among other benefits that will be discussed in the paper, one unique feature of our model is that it takes into consideration the effect of properties of particles (size and density, the former for the first time) to their vertical terminal velocity. With ocean current velocity taken from ECCOv4r4, a dataset generated from a data-assimilated MITgcm reanalysis, our model is integrated for 26 years for particles of different properties with their stationary patterns studied. We find that only low-density particles with sufficient size (e.g. density $900 kg/m^3$ with size $\gtrsim 10\mu m$) aggregate in the five subtropical gyres observed in previous studies. In contrast, particles of smaller size ($\sim 1\mu m$), irrespective of their density, behave like neutrally buoyant particles with a weaker pattern on the surface and a deeper penetration into depth (up to about 1km deep). In addition, we observe seasonal variations of floating particle concentration on the ocean surface, which reasonably agree with the satellite observation by Cyclone Global Navigation Satellite System (CYGNSS) in terms of the phase of the variation. We find that the seasonal variation of the surface particle concentration correlates well with the variation of the mixing layer (ML) depth globally, due to an almost uniform vertical distribution of particles in the ML with total amount of particles conserved.

Plain Language Summary

Oceanic plastic pollution is an urgent and global problem. We study the transport and distribution of microplastics (plastic pieces with sizes smaller than 5mm) through a newly developed computer simulation. In our simulations, the effect of plastic particle size is for the first time considered which affects the vertical motion of the particles together with their density. This consideration leads to new understanding of the microplastic stationary pattern compared to previous studies. For example, only plastic particles made from low-density material with sufficient size ($\gtrsim 10\mu m$) accumulate in the five subtropical gyres forming the garbage patch identified in previous studies. Small enough ($\sim 1\mu m$) plastic particles, on the other hand, exhibit weaker surface patterns and can be found in deeper ocean (up to about 1km deep). Additionally, we find that the amount of floating plastics on the sea surface changes seasonally, generally with more in summer and less in winter. This seasonal pattern agrees with the satellite observation by Cyclone Global Navigation Satellite System (CYGNSS), which consists of eight micro-satellites to measure, for example, wind speeds over Earth's oceans. We finally explain the seasonal variation and physically connect it to the variation of mixing layer depth of the ocean.

1 Introduction

Plastic pollution in the ocean is a fundamental environmental problem we face now and will face in the foreseeable future. An estimated eight million tons of plastic trash enters the ocean each year, and most of it is battered by sun and ocean waves into microplastics (i.e. plastic particles less than 5mm long according to a definition by NOAA on `https://marinedebris.noaa.gov/what-marine-debris/microplastics`). These micro pieces of plastics can easily enter the food chain and pollute the food we humans consume. Therefore, it is crucial to understand the distribution of microplastics in the global ocean for strategic removal of their pollution.

A major method for field measurements of oceanic plastic concentration is through trawler nets, which captures particles of size greater than 0.2mm floating near the ocean surface (Cózar et al., 2014; Eriksen et al., 2014). In spite of several successful attempts made using this approach, the information gained is too scarce in space and time. Moreover, the short length/time scale of the measurement also tends to make the results sensitive to inhomogeneous disturbances such as eddies and surface wind (Lebreton et al., 2012). Remote sensing methods, on the other hand, provide much greater spatial coverage. Among

several proposed techniques, Evans and Ruf (2022) retrieves the concentration of floating microplastics from the surface roughness anomaly (i.e. surface roughness lower than expected from wind), with the first microplastics database covering $38°S - 38°N$ established. While favorable agreement with other approaches have been reported, it should be noted that the retrieval algorithm relies on the presence of surfactant, instead of microplastics, to damp the surface roughness (Sun et al., 2023). Therefore, the results obtained need to be interpreted with caution on the difference of transport mechanisms between microplastics and surfactant.

Transport models of microplastics offer another way to understand their global distribution. Table 1 summarizes the existing global transport models, classified as 2D Lagrangian, 2D statistical and 3D Eulerian models. In 2D Lagrangian models, each particle released to the ocean is tracked as a passive scalar following the ocean surface current velocity, obtained from global reanalysis datasets (Chenillat et al., 2021; Lebreton et al., 2012). In 2D statistical models, the surface microplastics concentration is evolved taking into consideration the advection velocity in a probabilistic way, with the probability calculated from the Global Drifter Program (Niiler, 2001; van Sebille et al., 2012; Maximenko et al., 2012). Mountford and Morales Maqueda (2019) represents the first 3D Eulerian model which solves the advection-diffusion particle equation in the global ocean. The vertical movement of particles is also for the first time incorporated, which depends on both vertical convective motion of ocean flow and the buoyancy effect resulted from the density difference between particles and sea water. When these models are integrated for sufficient time, it is usually found that accumulation of particles, or low-density particles in Mountford and Morales Maqueda (2019), in five subtropical gyres appear as stationary patterns in the global ocean. However, it is not clear how this result is affected by particle size, which can affect the vertical motion of particles but is not considered in Mountford and Morales Maqueda (2019). In addition, some model results reveal seasonal variations of the surface particles (van Sebille et al., 2012), which is also observed in remote sensing data (Evans & Ruf, 2022), but a physical explanation of the phenomenon is lacking.

In this paper, we continue with the route of using Eulerian models to understand microplastics concentration in the global ocean. Indeed, not only have Eulerian models been extended to a 3D field, but also they have other benefits compared to Lagrangian models, e.g., the independence of computational cost on number of particles and extendable nature to incorporate particle fragmentation and data assimilation (as future work). Compared to Mountford and Morales Maqueda (2019), the Eulerian model developed for this paper is also associated with several advantages: (1) we formulate the buoyancy advection term in a mass-conserved manner, together with a formula for the vertical terminal velocity which incorporates the effect of particle size; (2) Our ocean current field is sourced from the Estimating the Circulation and Climate of the ocean Version 4, Release 4 (ECCOv4r4) dataset. In particular, ECCOv4r4 is established from a MITgcm (MIT general circulation model) global simulation from 1992 to 2017, with constrained data from Jason-3 satellite mission and the Ice-Tethered-Profiler (ITP) mission, just to mention a few. As a result, the velocity data exhibits higher fidelity (e.g., Stokes drift by surface waves partially captured because of the constraint by surface drifter data) and interannual variability, with both features not incorporated in Mountford and Morales Maqueda (2019). In addition, ECCOv4r4 is provided with a horizontal resolution of $40 - 100km$ and 50 vertical layers, and all our simulations are conducted at the same resolution which is almost two times finer in each spatial dimension than that in Mountford and Morales Maqueda (2019) (see Table 1).

Equipped with our new Eulerian model, we study the stationary distribution pattern of microplastics with different properties (i.e., density and size) after integration of the model from 1992 to 2017. We find that only positively buoyant particles with sufficient size (e.g., density $\rho = 900kg/m^3$ and diameter $d \gtrsim 10\mu m$) form patches in the five subtropical gyres observed in previous work. For small enough particles ($d \lesssim 1\mu m$) irrespective of their density, the distribution converges to that of neutrally buoyant particles with a much weaker

Table 1: Summary of features of our model and previous ones.

Models	Velocity data source	Resolution	Model type
Our model	ECCOv4r4[1]	$1/2° - 1°$	3D Eulerian
Chenillat et al. (2021)	GLORYS[2]	$1/12°$	2D Lagrangian
Mountford & Morales Maqueda (2019)	ORCA2-LIM3[3]	$1° - 2°$	3D Eulerian
Lebreton et al. (2012)	HYCOM[4]	$1/12°$	2D Lagrangian
van Sebille et al. (2012)	GDP[5]	$1°$	2D statistical
Maximenko et al. (2012)	GDP	$1°$	2D statistical

[1] Estimating the Circulation and Climate of the Ocean Version 4 Release 4.
[2] Global Ocean Physics Reanalysis.
[3] Nucleus for European Modelling of the Ocean Version 3.6, configuration ORCA2-LIM3.
[4] HYbrid Coordinate Ocean Model.
[5] Global Drifter Program.

surface accumulation pattern and a penetration into greater depth of about 1km. Additionally, for floating particles, we observe a seasonal variation of the surface concentration that reasonably agrees with remote sensing data from CYGNSS in terms of phase of the cycle. The seasonal variation of surface concentration is found to be well correlated with the seasonal variation of the mixing layer (ML) depth globally, based on which a physical explanation is developed. Specifically, as demonstrated in our model results, the floating particles have a nearly uniform distribution in the mixing layer due to the diffusion effect, and diminishes sharply at deeper depth. Because of the constant total mass of particles, their surface concentration varies inversely proportional to the depth of the ML (i.e., a column of uniformly distributed particles reacting to the variation of the ML depth).

This paper is organized as follows, in §2, we provide details of our microplastics transport model, including the model equations and formulation to incorporate the vertical motion and terminal velocity, as well as details of the ECCOv4r4 dataset. In §3, we show results of stationary patterns of plastic particles with different densities and sizes, with a focus on the effect of size to the distribution. The seasonal variation of the surface particles are discussed, in terms of its correlation with CYNGSS observation and the associated physical mechanism. §4 concludes the work and points out possible directions for further improvements.

2 Methodology

We model the microplastic particles as passive particles advected by the ocean current. Mathematically, the concentration of particles is described by an advection-diffusion equation with an additional term to represent the buoyancy effect:

$$\frac{\partial \tau}{\partial t} + \nabla \cdot (\tau \mathbf{u}) + \partial_z(\tau w_r) = \nabla \cdot (K \nabla \tau) + Q, \tag{1}$$

where τ is the particle concentration in g/m^3, $\nabla \equiv \frac{\partial}{\partial x}\hat{i} + \frac{\partial}{\partial y}\hat{j} + \frac{\partial}{\partial z}\hat{k}$ is the 3D gradient operator, with x, y, z the three spatial dimensions and $\hat{i}$, $\hat{j}$, $\hat{k}$ the unit vector in each dimension respectively, $\mathbf{u}$ is the ocean current velocity taken from the dataset ECCOv4r4 (described in detail in §2.1). The term $\partial_z(\tau w_r)$ represents the buoyancy effect with w_r, the vertical terminal velocity (described in §2.2). K is the 3×3 eddy diffusivity tensor, constructed by the summation of Gaspar-Grégoris-Lefevre (GGL) (Gaspar et al., 1990) and

Gent-McWilliams eddy & Redi (GMRedi) (Gent & Mcwilliams, 1990) parameterizations, the former modeling diapycnal diffusivity and latter accounting for corrections due to tilted isopycnals. In general, the two mixing schemes depend on the turbulent kinetic energy and sea water density distribution respectively, with both globally available from the ECCOv4r4 dataset. Finally, Q is the source term distributed along coastlines based on Jambeck's global mismanaged waste survey, consistent with the coastal input used in van Sebille et al. (2012) and Mountford and Morales Maqueda (2019).

In this work, equation (1) is solved using the 'ptracers' package in MITgcm, with necessary modifications to include the additional terms. Numerical setups for the simulation are summarized in §2.3, with key simulation files, result animations, and procedures made available and summarized in the section "Open Research Section". Animations of some simulation results are also uploaded as supplemental files.

2.1 ECCOv4r4 dataset

Estimating the Circulation and Climate of the Ocean Version 4 Release 4 (ECCOv4r4) provides a data-constrained ocean state reanalysis from 1992 to 2007 (ECCO Consortium et al., 2021, 2023; Forget et al., 2015). The backbone of this reanalysis is an MITgcm global simulation, together with a 4D-var technique to assimilate measurement data from sources such as Argo and OCCA (Ocean Comprehensible Atlas) (Toole et al., 2011; Forget, 2010). The MITgcm simulation is conducted in hydrostatic mode on the so-called ECCO-LLC90 grid, which has about $1°$ horizontal resolution (corresponding to $40 - 100km$ grid size) with further meridional refinement and 50 vertical layers with $10 - 500m$ resolution. A time step of $1hr$ is used which ensures the stability of the simulation. Parameters such as initial conditions and forcing (biweekly averaged surface wind stress, radiative heat flux, etc.) are set as variables, through the tuning of which the difference between the simulation and measurements are minimized as in the 4D-var technique.

We take the ocean current velocity $\mathbf{u}$ from ECCOv4r4 to feed the simulation of equation (1). Such a velocity field contains resolved physics such as geostrophic and the Ekman current components, as well as other components captured in an indirect way. For example, surface wave induced Stokes drift is partially captured due to the adjustment of wind shear stress to fit the data from surface drifter as part of the data assimilation (Reynolds et al., 2002). In addition, MITgcm simulation also includes an equation for turbulent kinetic energy (with parameterized production and dissipation) which provides information to calculate the GGL parameterization of diffusivity in equation (1) and for temperature and salinity.

2.2 Buoyancy advection term

The buoyancy effect of particles is modeled by a term in advection form, $\partial_z(\tau w_r)$, in equation (1). This is because a particle falling/rising with its terminal velocity w_r is equivalent to the particle being advected by an "external" velocity w_r. We note that this buoyancy advection term has to be in a mass-conservative form, in the sense that if there is no flux (or balanced flux) from the upper and lower boundary the mass in the domain should stay constant. This property is satisfied only when the term is written as $\partial_z(\tau w_r)$ instead of $w_r \partial_z \tau$. In Mountford and Morales Maqueda (2019), the latter form is used at least judged from their presented equation, which may result in inconsistency in some presented results.

We now discuss the formula of w_r dependent on both the particle size and density, as presented in Yang et al. (2014) and Dey et al. (2019). Consider a spherical particle of diameter d at terminal velocity w_r subject to buoyancy force $B = g(\rho_w - \rho_p)(4\pi/3)(d/2)^3$ and drag force $D = C_D(1/2)(\rho_w w_r^2)\pi(d/2)^2$, with their balance leading to

$$w_r^2 C_D = \frac{4}{3}dg\frac{\rho_w - \rho_p}{\rho_w}, \tag{2}$$

where g is the gravitational acceleration, ρ_w is the water density, ρ_p is the particle's mass density, C_D is the drag coefficient that depends on the particle Reynolds number $Re \equiv \rho_w dw_r/\mu$, with μ the dynamic viscosity of sea water. For typical size ($< 0.1mm$) and velocity ($< 1mm/s$) of microplastics, we have $Re = O(0.1) < 1$. At this regime of Re, it has been shown that $C_D = 24/Re$ irrespective of the shape of the particle. Therefore, the final formula can be written as

$$w_r = \frac{g(\rho_w - \rho_p)d^2}{18\mu},\tag{3}$$

which we use in the simulation of equation (1). As an example, consider biomaterial particles like phytodetritus, typically at mass density $1388kg/m^3$ (Kooi et al., 2017). The formula (3) gives sinking velocity $42.7m/day$ and $170.9m/day$ for particles at $50\mu m$ and $100\mu m$ respectively, which is comparable to the measurement of at least $64m/day$ in the marine snow event after the 2011 Tohoku–Oki Earthquake (although the size of particles in the measurement is not specified) (Oguri et al., 2013). In addition, based on the buoyancy and drag forces to accelerate the particles, the typical time for a microplastic particle to reach terminal velocity is below 1s (see Appendix A for a detailed analysis). As a result, the acceleration process can be safely neglected in our model with the total integration time of 26 years.

2.3 Numerical and Case Setup

We numerically integrate equation (1) with a finite volume method using the MITgcm "ptracers" package with additional implementation of the buoyancy advection term. The computation is performed on the ECCO-LLC90 grid with the same resolution and time step as those to generate the ECCOv4r4 dataset. At all boundaries, zero flux boundary condition (including the flux due to w_r) is applied. Since MITgcm simulation is conducted with a variable free surface (instead of a rigid lid), the thickness of cells need to be changed at each time step to accommodate the variation of free surface. This is treated through a mapping technique presented in Adcroft and Campin (2004); Campin et al. (2004). The Q term in equation (1) is handled by the "gchem" package, with positive values in g/m^3s converted from the mismanaged weight and distributed in the surface cells along the coastlines. In the situation where a cell is cut by the coastline, a "partial-step" method is applied to account for the situation (Adcroft et al., 1997). A map of Q on the ECCO-LLC90 grid is provided in figure 1.
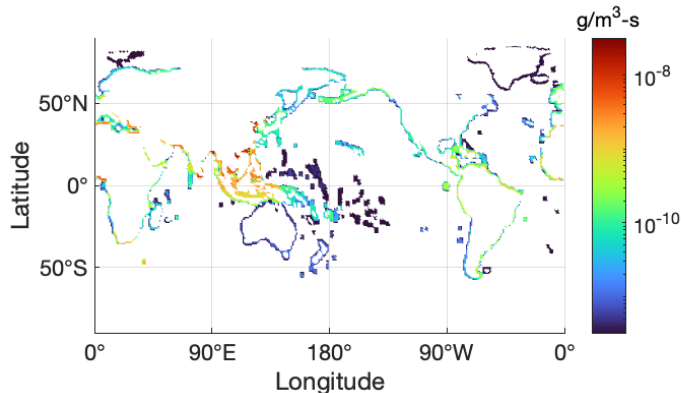

Figure 1: Map of Q on the ECCO-LLC90 grid, based on the waste management report (Jambeck et al., 2015).

Table 2: Summary of particle properties in the two idealistic and six realistic cases. A typical value of terminal velocity is estimated based on a sea water density $1025 kg/m^3$.

Particle label	Mass density(kg/m^3)	Diameter (μm)	$w_r(\rho_w = 1025 kg/m^3)$
2D surface	NA	NA	NA
Neutrally buoyant	NA	NA	0
PE-10	900	10	$6.3 \mu m/s$
PE-1	900	1	$0.06 \mu m/s$
PP-100	1030	100	$-27.3 \mu m/s$
PP-10	1030	10	$-0.27 \mu m/s$
PVC-10	1200	10	$-9.5 \mu m/s$
PVC-1	1200	1	$-0.09 \mu m/s$

Note: typical vertical ocean current has magnitude around $5 \mu m/s$.

We consider two idealistic cases and six realistic cases as summarized in Table 2, with the former providing insight on the particle behavior under extreme conditions and the latter aiming to understand the effect of particle properties on the distribution. The first idealistic case is when the problem is reduced to two dimensions (2D), which is an extreme case for particles with sufficiently high buoyancy ($w_r \to \infty$) so that they stay on the top layer near the free surface. This case is practically simulated by setting the third component of both **u** and gradient operator, as well as w_r, to be zero in equation (1). It can be hypothesized that the 2D idealistic case leads to strong gyre patterns since particle accumulation in converging flow zone in the ocean cannot be reduced by the corresponding vertical downward flow as in 3D cases. For an analytical solution of 2D accumulation, see Maximenko et al. (2012). The second idealist case is for neutrally buoyant particles to represent those with $d \to 0$ so that $w_r \to 0$. The six realistic cases are conducted for three types of plastics (PE for Polyethylene, PP for Polypropylene, and PVC for Polyvinyl Chloride) with densities lower than, comparable to and higher than sea water, respectively. For each particle density, two particle sizes are considered for their distinguished behavior in the stationary distribution.

3 Results

3.1 Idealistic cases

We first present results for the 2D idealistic cases in figure 2, which shows the surface concentration of particles averaged over the last year of the 26-year simulation. Together with our results we also provide in Appendix B a graphical comparison to results from previous 2D studies in Maximenko et al. (2012), Lebreton et al. (2012), van Sebille et al. (2012), and Chenillat et al. (2021). It can be seen that our result reproduces accumulation in the five subtropical gyres at North Pacific, South Pacific, North Atlantic, South Atlantic, and Indian Ocean found in previous works. In addition, we observe another accumulation in the north Arctic area which is not present in aforementioned previous studies (for some of them because the ocean current data, say from GDP, does not well cover the arctic area). However, gyre accumulation patterns at the arctic have indeed been observed (although weaker) in the 3D Eulerian model for positively buoyant particles as shown in Mountford and Morales Maqueda (2019) (see their figure 3). In general, our results shown here is also a confirmation about our hypothesis in §2.3 on the strong gyre accumulation pattern for the 2D case.

We next show results for the case with neutrally buoyant particles in figure 3, (a) for surface concentration and (b) for concentration at a vertical slice of $38°S$ up to $1km$
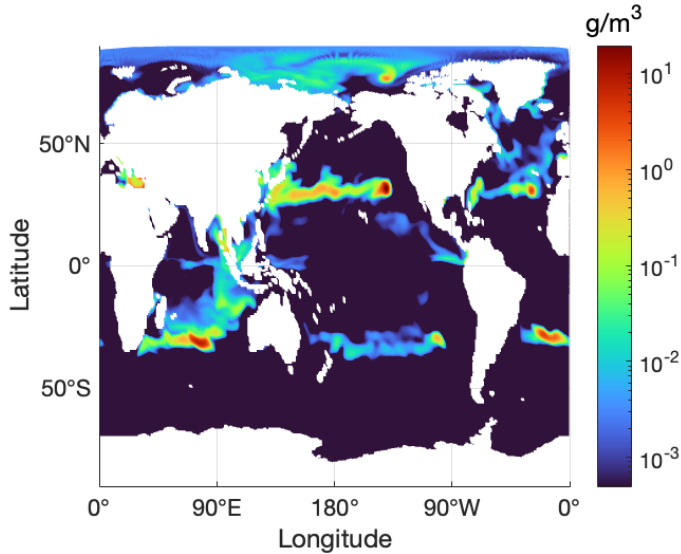
Figure 2: Surface particle concentration in the 2D idealistic case, averaged over the last year of the 26-year simulation.

depth to reveal the vertical distribution. A graphical comparison of this result to that in Mountford and Morales Maqueda (2019) is also provided in Appendix B. It can be seen from figure 3a that the gyre accumulation pattern is much weaker in this case compared to the 2D result, with some weak accumulations present in North Pacific, North Atlantic, South Atlantic, and Indian Ocean, but not South Pacific. The vertical distribution in figure 3b shows that the particles penetrate downward up to about $1km$ depth, much deeper than the mixing layer depth of about $200m$. This penetration could be due to the diapycnal mixing present ubiquitously everywhere in the ocean interior. We will use the results in figure 3 as a reference to understand the distribution of realistic particles with sufficiently small size in following discussions.

3.2 Realistic cases

3.2.1 *Positively buoyant particles*

Polyethylene (PE) is a plastic material with density lower than the sea water. Here we take a representative density of $900kg/m^3$, and two particle sizes of $10\mu m$ (PE-10) and $1\mu m$ (PE-1). Snapshots of the yearly-averaged solutions at the end of 26-year simulations for both particle sizes are shown in figures 4, in terms of surface concentration and vertical distributions.

For PE-10 (i.e. larger particles), we see clear accumulation of particles in the five gyres identified in the 2D results, as well as some particle concentration in the Arctic ocean similar to figure 2. As expected, the concentration in the gyres is generally weaker than those shown in figure 2 (note that different color bars are used) due to the vertical downwelling motion in the 3D cases. From figure 4c, we find that the majority of particles stay close to the sea surface within 200m depth, i.e., the depth of ocean mixing layer. For PE-1 (i.e., smaller particles), in contrast, the accumulation in gyres becomes weaker and distributions shown in figures 4b and 4d are visually identical to the neutrally buoyant cases shown in figure 3. A quantitative comparison between PE-1 and neutrally buoyant cases reveals some small
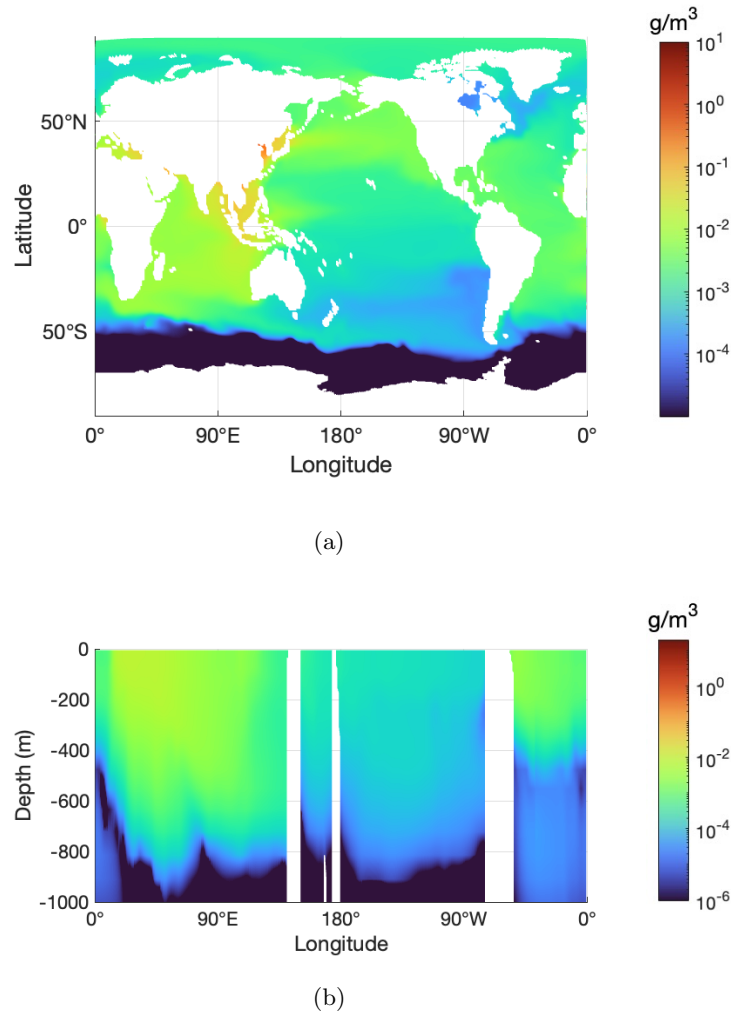
(a)

(b)

Figure 3: Particle distribution in the case of neutrally buoyant particles, averaged over the last year of the 26-year simulation, in terms of concentration (a) on the surface and (b) over a vertical slice at $38°S$ and upper 1km of the ocean.

difference in the concentration within the upper $500m$ of surface water. Indeed, for PE-1, the terminal velocity is $0.06\mu m/s$, which at most results in $50m$ upward shift of the particles in the 26 years of evolution.

Comparing results regarding PE-10 and PE-1, we find that larger particles are more likely to be accumulated in the gyres close to the surface. Therefore, ocean surface serves as a filter on the size of PE particles in the sense that larger particles are present in the gyres and smaller particles are "sifted" downward by the vertical mixing process. In the previous trawler experiments collecting the surface particles, it should be expected that most of particles with a similar density as PE are with a size above some threshold.
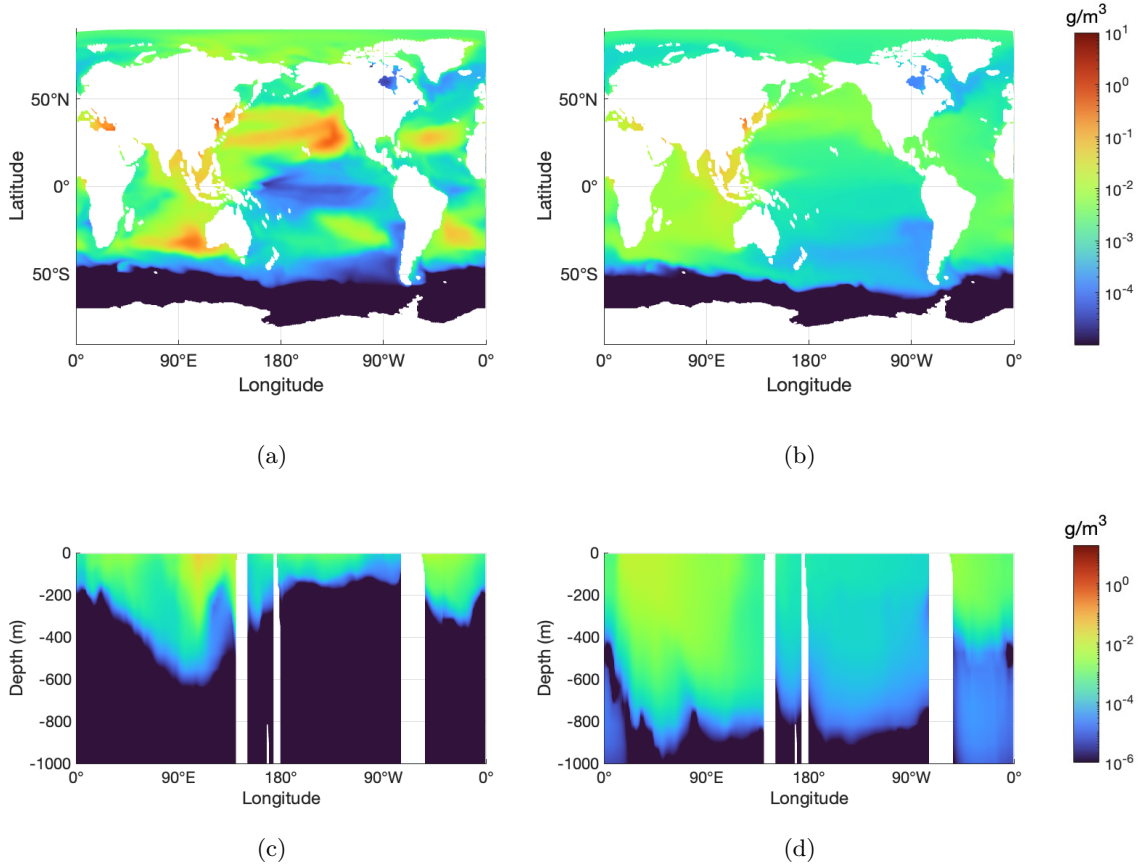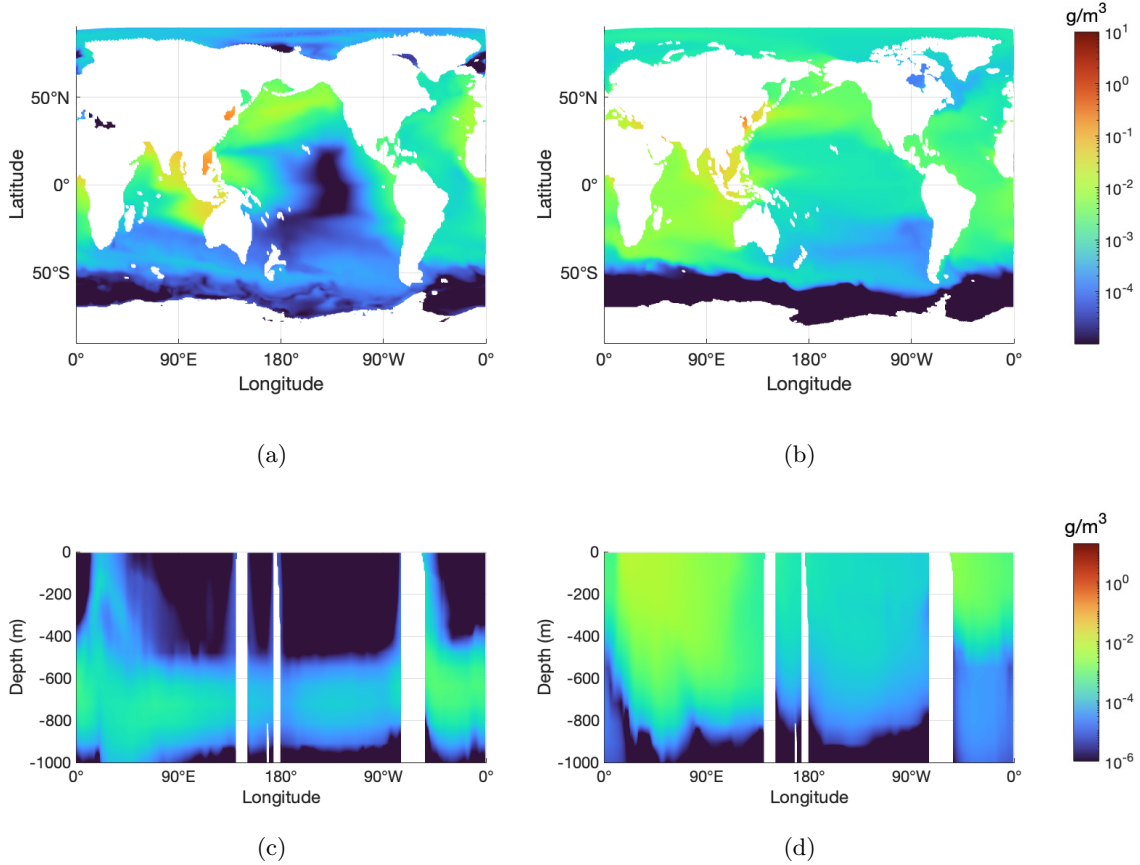
Figure 4: Particle distribution of PE particles of two sizes, averaged over the last year of the 26-year simulation. The distribution of PE-10 is shown in terms of concentration (a) on the surface and (c) over a vertical slices at $38°S$, and the counterpart for PE-1 is shown in (b) and (d).

3.2.2 Particles with density close to sea water

Polypropylene (PP) is a plastic material with a density comparable to sea water. We take a representative density of $1030 kg/m^3$, in two sizes of $10\mu m$ (PP-10) and $100\mu m$ (PP-100), with the simulation results shown in figure 5. The PP-100 particles are mostly concentrated, as shown in figure 5c, at a depth of about $650m$ where the local sea water density is close to particle density. This is a stable state for the stationary distribution since the PP-100 particles with any deviation from this depth tend to be returned to the depth by the buoyancy restoring effect (with a water density increasing with depth in the stably stratified state). At this depth of $650m$, the particle concentration is plotted in figure 5a, which shows high concentration in regions close to the coast. This is because the particles released at the coastlines are advected horizontally to the open ocean and in the meanwhile sink vertically due to the buoyancy effect. As they reach about $650m$ depth, the horizontal advection almost vanishes due to small horizontal ocean flow motion at that depth. Therefore, there exists a time scale $T_s \approx 9\ months$ determined by the time of particles sinking to the stationary layer, beyond which the particles are not further advected to the open ocean.

For the PP-10 results shown in figures 5b and 5d, in contrast, the distribution becomes similar to that in the neutrally buoyant case. We note that for density of $1030kg/m^3$, $10\mu m$ is demonstrated to be the critical size for the neutrally buoyant behavior to occur, whereas for PE density of $900kg/m^3$ discussed in §3.2.1, the critical size goes down to $1\mu m$. This can be understood from equation (3), where w_r can be made sufficiently small from either a small particle size d or small density difference $\rho_w - \rho_p$. In addition, for the PP density, the ocean surface serves as a filter with an opposite effect to that for the PE density, in the sense that only small particles are expected to be found in trawler experiments at the ocean surface.
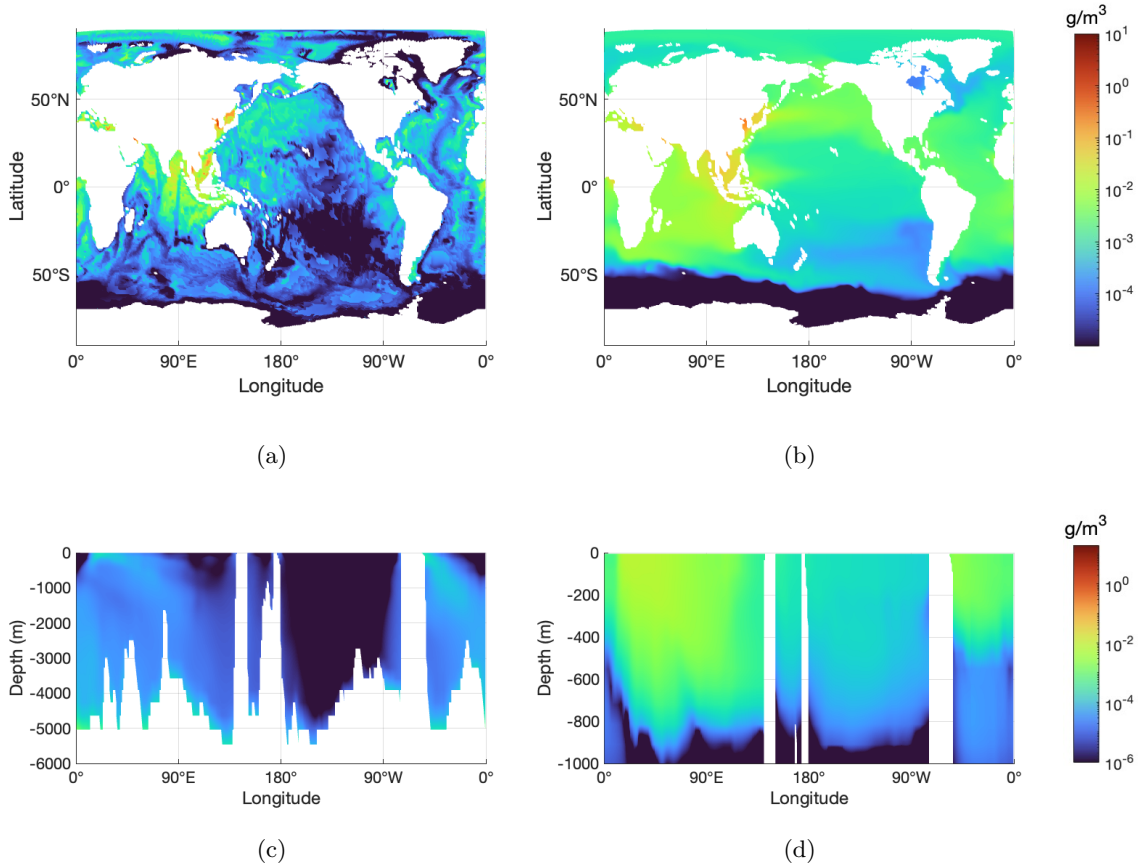

Figure 5: Particle distribution of PP particles of two sizes, averaged over the last year of the 26-year simulation. The distribution of PP-100 is shown in terms of concentration (a) at $-650m$ depth and (c) over a vertical slices at $38°S$. The distribution of PP-10 is shown in terms of concentration (b) on the surface and (d) over a vertical slices at $38°S$.

3.2.3   High-density particles

Polyvinyl chloride (PVC) is a plastic material with a density significantly higher than sea water. We take a representative density of $1200kg/m^3$ which is higher than the sea water density in the range of $1000 < \rho_w < 1050kg/m^3$. Figure 6 shows the results for two particle sizes $10\mu m$ (PVC-10) and $1\mu m$ (PVC-1). At the end of the 26-year simulation, most PVC-10 particles, as demonstrated in figure 6c, sink to the sea bottom and accumulate in the ocean trenches. However, there are some concentration of particles present over all

depth as seen in figure 6c, which are from particles released from the coastline and in their process to sink to the bottom. We note that for PVC-10, it takes $T_s \approx 20 \; years$ for them to sink to the sea bottom with $w_r = -9.5 \mu m/s$. This value of T_s is much longer than that for PP-100, so that particles over all depth in figure 6c is more evident than that in figure 5c (since the PVC-10 particles have more time to travel horizontally before sinking to the bottom). Figure 6a shows the sea bottom concentration of PVC-10 particles, which demonstrates higher concentration near the coastline similar to PP-100 in figure 5, but with a greater horizontal spreading for PVC-10 particles.

For PVC-1, as shown in figure 6b and 6d, the particle distribution again becomes similar to that of neutrally buoyant particles. A terminal vertical velocity of $w_r \approx 0.09 \mu m/s$ results in a downshift of $78 m$ in 26 years, which only slightly shifts down the concentration of PVC-1 compared to neutrally buoyant particles. As a result, the ocean surface serves as a filter in the same way as that for the PP particles.

Figure 6: Particle distribution of PVC particles of two sizes, averaged over the last year of the 26-year simulation. The distribution of PVC-10 is shown in terms of concentration (a) at the ocean bottom and (c) over a vertical slices at $38°S$ covering all ocean depth. The distribution of PVC-1 is shown in terms of concentration (b) on the surface and (d) over a vertical slices at $38°S$ covering only the upper $1 km$ depth.

3.3 Seasonal variation of surface concentration

Seasonal variation of particle concentrations have been revealed in remote sensing data from CYGNSS (Evans & Ruf, 2022), and later also recorded from the previous numerical study (Mountford & Morales Maqueda, 2019). In this section, we focus on the variation of surface concentration for which the most important plastic particles are those like PE-10. Figure 7 shows the variation of τ of PE-10 averaged over the North Pacific Ocean for 5 years, where we can see the variation within each year (i.e. seasonal variation) as well as variations over a longer time scale. It is the seasonal variation that we are interested in here.
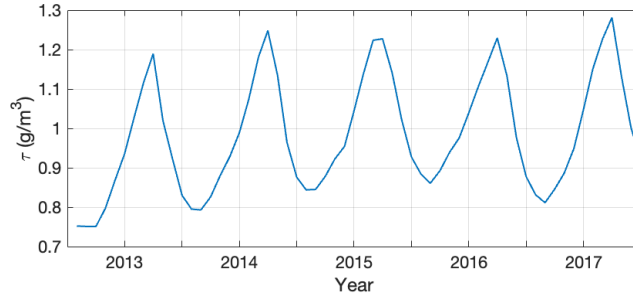
Figure 7: Surface concentration of PE-10 microplastics averaged over the North Pacific $[20°N - 35°N, 130°W - 150°E]$ across 5 years. In general, concentration is higher in summer and lower in winter.

We first perform a comparison between our model data and CYGNSS observation in terms of the phase of the seasonal cycle. For this purpose, we define the peak time, T_p, as the month within a year when maximum value of τ is recorded on the ocean surface. Figure 8 shows maps of T_p between $38°S$ and $38°N$ (i.e., the covered region of CYGNSS measurement) in year 2017 from both our model data and CYGNSS data. In particular, the CYGNSS result is computed from the version 1.0 CYGNSS level 3 ocean microplastics concentration data at $1/4°$ resolution. We see that the comparison in figure 8 shows reasonable (first-order) agreement, e.g., in terms of peak concentration in summer in the subtropical bands of both the Northern and Southern hemispheres. Of course, certain level of discrepancy exists, which should be understood taking consideration of many factors. For example, CYGNSS retrieves the microplastic concentration from the surface roughness, which is dominantly affected by surfactant (Sun et al., 2023) (along with other factors such as precipitation and sea surface air pressure), which may have a different seasonal variation mechanism from plastic particles.

We next turn to the physical mechanism leading to the seasonal variation of τ at the ocean surface. Here we consider three candidate quantities that may be related to the seasonal variation of τ: The first one is the horizontal divergence of the surface water, $\nabla_h \cdot \mathbf{u}_h$, which serves as an indication of flow convergence zone or gyres at the surface. The second one is the Ekman upwelling/downwelling velocity, w_E, which can move the particles up and down in the Ekman layer and thus relevant. The Ekman velocity can be computed by taking the curl of surface wind stress (available in ECCOv4r4), which induces a surface motion associated with a vertical flow from continuity (Risien & Chelton, 2008). The third one is the ocean mixing layer (ML) depth, h_b, which affects the vertical mixing of particles. In practice, we compute h_b as the depth where the buoyancy frequency is maximized, i.e., the density gradient is maximized under Boussinesq approximation (Gaspar et al., 1990). Figure 9 shows two-year time series of the three candidate quantities together with τ at
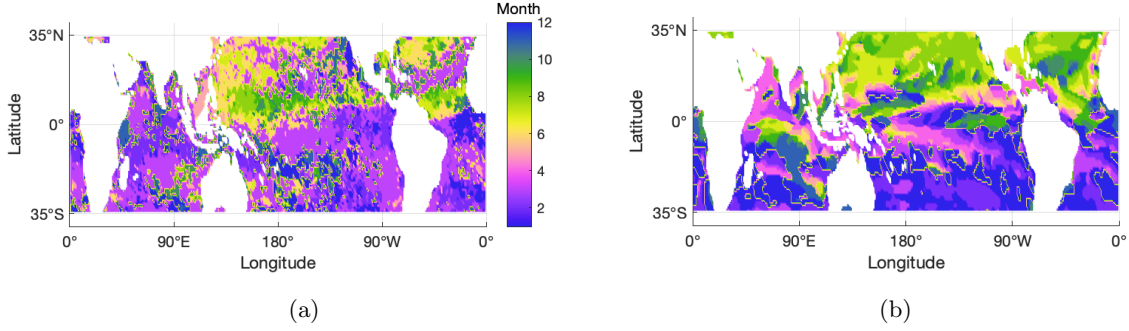
Figure 8: Map of T_p from (a) CYGNSS observation and (b) the PE-10 model result. The color denotes months 1-12, meaning January-December of a calendar year.

$[30°N, 130°W]$ in the North Pacific gyre, where we see indeed that all three quantities exhibit seasonal variations.
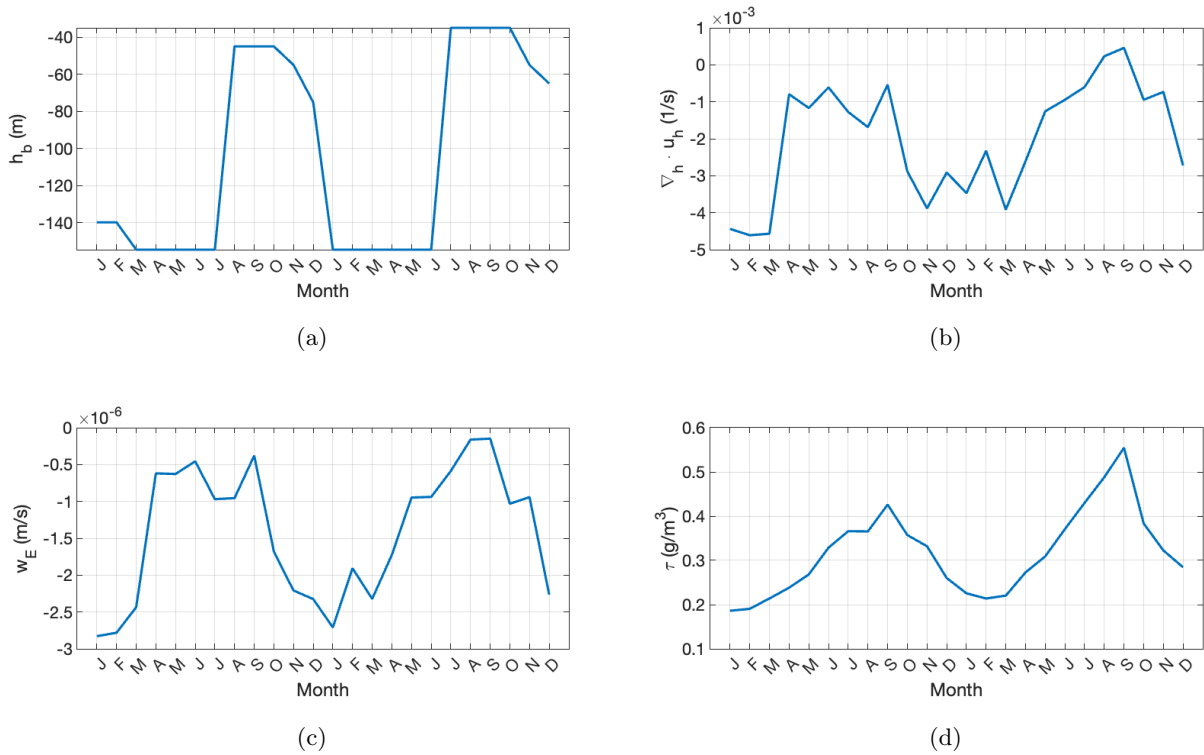

Figure 9: Two years of seasonal cycle of (a) mixed layer depth h_b, (b) ocean current horizontal divergence $\nabla_h \cdot \mathbf{u}_h$, (c) Ekman upwelling velocity w_E, and (d) surface concentration τ, all taken at $[30°N, 130°W]$ in the North Pacific gyre.

To understand which candidate quantity is most relevant to the seasonal variation of τ, we examine the correlation coefficient between surface τ and each of the three quantities.

We plot in figure 10 three global maps of these correlation coefficients, computed for years 2012 through 2017. It is clear that h_b is the most correlated factor, which shows positive correlation coefficient close to 1 in almost all locations in the map. On the other hand, while $\nabla_h \cdot \mathbf{u}_h$ and w_E may be important in forming particle accumulation in gyres, they are not critical for the particle seasonal variation observed.
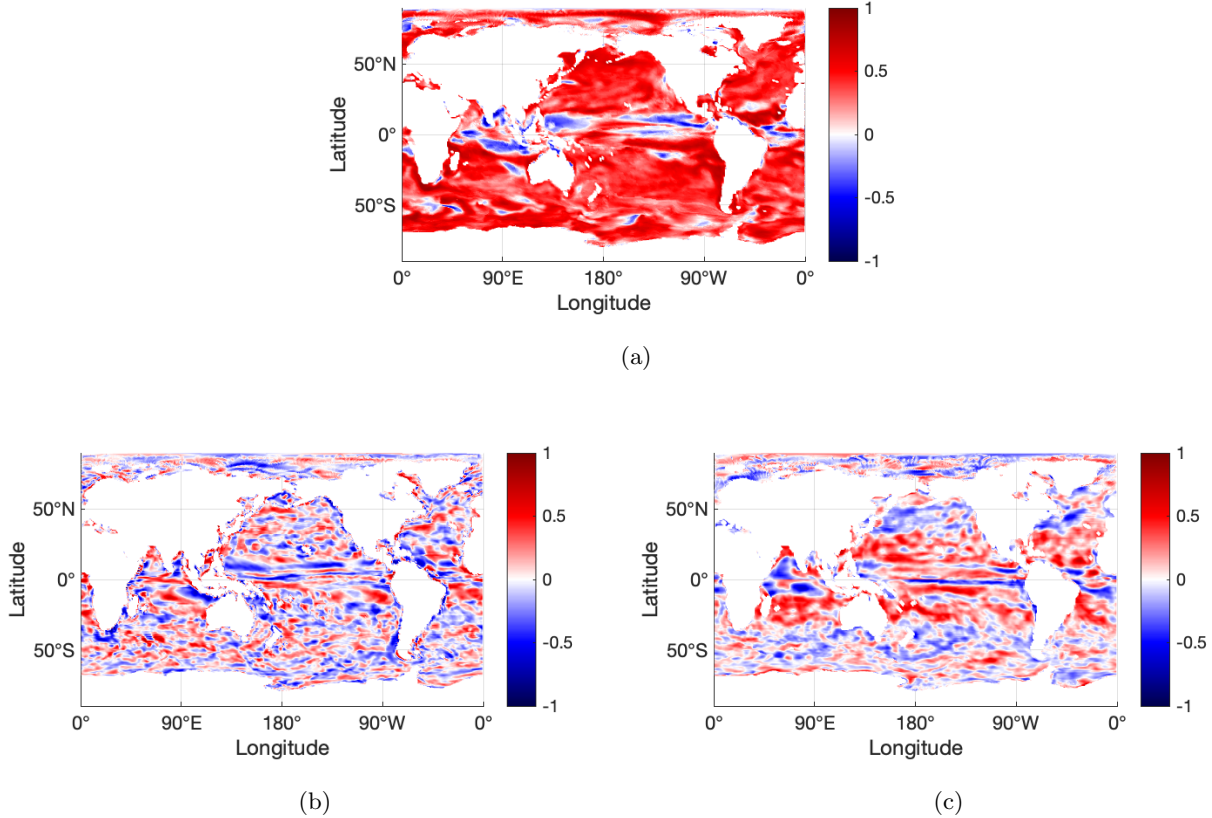

(a)

(b)

(c)

Figure 10: Maps of correlation coefficients computed over six years (2012-2017) between the surface concentration τ and (a) the mixed layer depth h_b, (b) the horizontal divergence of surface current $\nabla_h \cdot \mathbf{u}_h$, and (c) the Ekman upwelling velocity w_E.

The globally favorable correlation between τ and h_b can be physically explained by the mixing behavior of particles in the ML. Positively buoyant particles such as PE-10 are well mixed in the ML and diminishes rapidly below that as already demonstrated in figure 4c. It can be expected that as h_b varies seasonally, the particle concentration varies (inversely proportional to h_b) conserving the total amount of particles. To confirm this explanation, we plot in figure 11 the concentration τ on a vertical slice at $[30°N, 130°W]$ in July (with higher surface concentration) and December (with lower surface concentration). It can be seen that almost uniform concentration is achieved in both July and December with different ML depths, resulting in the different values of τ at the ocean surface.

4 Conclusion and discussion

We develop a 3D Eulerian model to study microplastic distribution in the global ocean, where the buoyancy effect of the plastic particles is incorporated through a terminal velocity
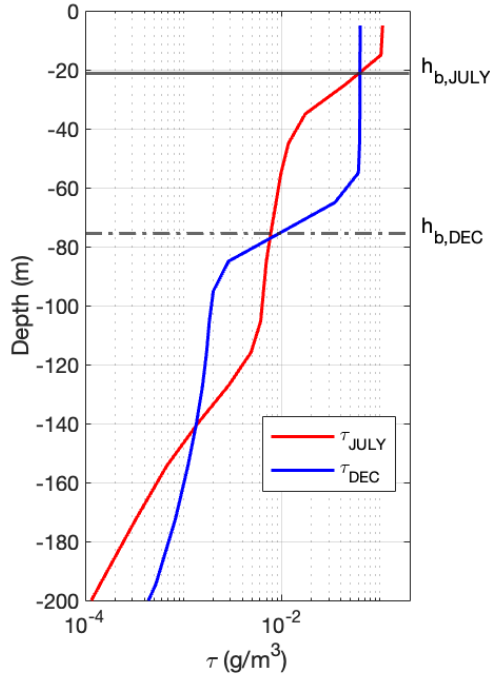
Figure 11: Vertical profile of the PE-10 plastic distribution taken at $[30°N, 130°W]$ in July 2017 (red) and December 2017 (blue). The mixed layer depth are indicated in July by solid black line and in December by dashed black line.

convection term formulated in a mass-conservative way. The terminal velocity depends on both the density and size of the particles, with the latter studied for the first time in this paper. Among the six representative types of particles studied, only positively buoyant particles with sufficient size (e.g., PE with diameter $d = 10\mu m$) accumulate in the five subtropical gyres, forming the garbage patches suggested by earlier works. For all plastic materials studied, as the particle size decreases below a threshold ($\lesssim 1\mu m$ for PE and PVC, $\lesssim 10\mu m$ for PP), their distribution converges to that of neutrally buoyant particles, exhibiting weaker accumulation on the surface with a deeper vertical penetration to about 1km. Examination of particle surface concentration also identifies the ocean surface as a filter for particle sizes that behaves differently for different particle densities. In addition, we study the seasonal variation of surface concentration of floating particles (PE-10), which shows reasonable agreement with CYGNSS observation in its covered area in terms of the phase of the seasonal cycle. We further find that this seasonal variation correlates well with the seasonal variation of the ML depth, leading to a physical explanation that the variation of surface concentration is due to a uniform concentration of particles in the ML which changes with the change of ML depth.

The development of our current model opens a new door for further improvement. Our next goal is to consider simultaneously particles of different densities and sizes, together with models for fragmentation and biofouling. In particular, the fragmentation and biofouling will serve as dissipation mechanisms for surface particle concentration, since the former reduces particle sizes and the latter increases particle density. After these processes are included, we plan to develop a data assimilation interface for the model to consider remote-sensing and trawler measurement data. By tuning parameters in the model (e.g., those related to fragmentation/biofouling, coastal input, etc.), we aim to minimize the model-to-

measurement error in a certain form. The final goal is to produce a data-constrained model outputs of microplastic concentration that covers different plastic types and particle sizes.

Open Research Section

To reproduce simulations in this paper, one can follow five procedures briefly summarized below.

1. Download MITgcm package.
2. Download ECCOv4r4 dataset (in particular the forcing and initial conditions for MITgcm to reproduce the ECCOv4r4 dataset).
3. Download additional code (used in step 4) and inputs (used in step 5) at `https://github.com/zizien1019/reproduce_eccov4r4_online_68o` to treat additional terms in equation (1). Animations of some simulation results are also provided in the repository.
4. Compile both the original MITgcm code and additional code in step 3.
5. Conduct simulations with different inputs on particle properties.

A file uploaded at `https://github.com/zizien1019/reproduce_eccov4r4_online_68o/blob/main/Read_me.pdf` contains much more detailed step-by-step instructions.

References

Adcroft, A., & Campin, J.-M. (2004, jan). Rescaled height coordinates for accurate representation of free-surface flows in ocean circulation models. *Ocean Modelling*, *7*(3–4), 269–284. Retrieved from `http://dx.doi.org/10.1016/j.ocemod.2003.09.003` doi: 10.1016/j.ocemod.2003.09.003

Adcroft, A., Hill, C., & Marshall, J. (1997, sep). Representation of topography by shaved cells in a height coordinate ocean model. *Monthly Weather Review*, *125*(9), 2293–2315. Retrieved from `http://dx.doi.org/10.1175/1520-0493(1997)125<2293:ROTBSC>2.0.CO;2` doi: 10.1175/1520-0493(1997)125⟨2293:rotbsc⟩2.0.co;2

Campin, J.-M., Adcroft, A., Hill, C., & Marshall, J. (2004, jan). Conservation of properties in a free-surface model. *Ocean Modelling*, *6*(3–4), 221–244. Retrieved from `http://dx.doi.org/10.1016/S1463-5003(03)00009-X` doi: 10.1016/s1463-5003(03)00009-x

Chenillat, F., Huck, T., Maes, C., Grima, N., & Blanke, B. (2021, apr). Fate of floating plastic debris released along the coasts in a global ocean model. *Marine Pollution Bulletin*, *165*, 112116. Retrieved from `http://dx.doi.org/10.1016/j.marpolbul.2021.112116` doi: 10.1016/j.marpolbul.2021.112116

Cózar, A., Echevarría, F., González-Gordillo, J. I., Irigoien, X., Úbeda, B., Hernández-León, S., ... Duarte, C. M. (2014, jun). Plastic debris in the open ocean. *Proceedings of the National Academy of Sciences*, *111*(28), 10239–10244. Retrieved from `http://dx.doi.org/10.1073/pnas.1314705111` doi: 10.1073/pnas.1314705111

Dey, S., Zeeshan Ali, S., & Padhi, E. (2019, aug). Terminal fall velocity: the legacy of stokes from the perspective of fluvial hydraulics. *Proceedings of the Royal Society A: Mathematical, Physical and Engineering Sciences*, *475*(2228), 20190277. Retrieved from `http://dx.doi.org/10.1098/rspa.2019.0277` doi: 10.1098/rspa.2019.0277

ECCO Consortium, Fukumori, I., Wang, O., Fenty, Heimbach, P., & Ponte, R. M. (2021, feb). Synopsis of the ecco central production global ocean and sea-ice state estimate, version 4 release 4. Retrieved from `https://zenodo.org/record/4533349` doi: 10.5281/ZENODO.4533349

ECCO Consortium, Fukumori, I., Wang, O., Fenty, Heimbach, P., & Ponte, R. M. (2023, jun). *Ecco central estimate (version 4 release 4)*. Retrieved from `https://ecco.jpl.nasa.gov/drive/files/Version4/Release4`

Eriksen, M., Lebreton, L. C. M., Carson, H. S., Thiel, M., Moore, C. J., Borerro, J. C., ... Reisser, J. (2014, dec). Plastic pollution in the world's oceans: More than 5

trillion plastic pieces weighing over 250,000 tons afloat at sea. *PLoS ONE*, *9*(12), e111913. Retrieved from `http://dx.doi.org/10.1371/journal.pone.0111913` doi: 10.1371/journal.pone.0111913

Evans, M. C., & Ruf, C. S. (2022). Toward the detection and imaging of ocean microplastics with a spaceborne radar. *IEEE Transactions on Geoscience and Remote Sensing*, *60*, 1–9. doi: 10.1109/TGRS.2021.3081691

Forget, G. (2010, jun). Mapping ocean observations in a dynamical framework: A 2004–06 ocean atlas. *Journal of Physical Oceanography*, *40*(6), 1201–1221. Retrieved from `http://dx.doi.org/10.1175/2009JPO4043.1` doi: 10.1175/2009jpo4043.1

Forget, G., Campin, J.-M., Heimbach, P., Hill, C. N., Ponte, R. M., & Wunsch, C. (2015, oct). Ecco version 4: an integrated framework for non-linear inverse modeling and global ocean state estimation. *Geoscientific Model Development*, *8*(10), 3071–3104. Retrieved from `http://dx.doi.org/10.5194/gmd-8-3071-2015` doi: 10.5194/gmd -8-3071-2015

Gaspar, P., Grégoris, Y., & Lefevre, J. (1990, sep). A simple eddy kinetic energy model for simulations of the oceanic vertical mixing: Tests at station papa and long-term upper ocean study site. *Journal of Geophysical Research: Oceans*, *95*(C9), 16179–16193. Retrieved from `http://dx.doi.org/10.1029/JC095iC09p16179` doi: 10.1029/jc095ic09p16179

Gent, P. R., & Mcwilliams, J. C. (1990, jan). Isopycnal mixing in ocean circulation models. *Journal of Physical Oceanography*, *20*(1), 150–155. Retrieved from `http://dx.doi.org/10.1175/1520-0485(1990)020<0150:IMIOCM>2.0.CO;2` doi: 10.1175/1520-0485(1990)020⟨0150:imiocm⟩2.0.co;2

Jambeck, J. R., Geyer, R., Wilcox, C., Siegler, T. R., Perryman, M., Andrady, A., … Law, K. L. (2015, feb). Plastic waste inputs from land into the ocean. *Science*, *347*(6223), 768–771. Retrieved from `http://dx.doi.org/10.1126/science.1260352` doi: 10.1126/science.1260352

Kooi, M., Nes, E. H. v., Scheffer, M., & Koelmans, A. A. (2017, jun). Ups and downs in the ocean: Effects of biofouling on vertical transport of microplastics. *Environmental Science & Technology*, *51*(14), 7963–7971. Retrieved from `http://dx.doi.org/10 .1021/acs.est.6b04702` doi: 10.1021/acs.est.6b04702

Lebreton, L.-M., Greer, S., & Borrero, J. (2012, mar). Numerical modelling of floating debris in the world's oceans. *Marine Pollution Bulletin*, *64*(3), 653–661. Retrieved from `http://dx.doi.org/10.1016/j.marpolbul.2011.10.027` doi: 10.1016/j.marpolbul .2011.10.027

Maximenko, N., Hafner, J., & Niiler, P. (2012, jan). Pathways of marine debris derived from trajectories of lagrangian drifters. *Marine Pollution Bulletin*, *65*(1–3), 51–62. Retrieved from `http://dx.doi.org/10.1016/j.marpolbul.2011.04.016` doi: 10 .1016/j.marpolbul.2011.04.016

Mountford, A. S., & Morales Maqueda, M. A. (2019, dec). Eulerian modeling of the three-dimensional distribution of seven popular microplastic types in the global ocean. *Journal of Geophysical Research: Oceans*, *124*(12), 8558–8573. Retrieved from `http://dx.doi.org/10.1029/2019JC015050` doi: 10.1029/2019jc015050

Niiler, P. (2001). The world ocean surface circulation. In *Ocean circulation and climate - observing and modelling the global ocean* (p. 193–204). Elsevier. Retrieved from `http://dx.doi.org/10.1016/S0074-6142(01)80119-4` doi: 10.1016/s0074 -6142(01)80119-4

Oguri, K., Kawamura, K., Sakaguchi, A., Toyofuku, T., Kasaya, T., Murayama, M., … Kitazato, H. (2013, may). Hadal disturbance in the japan trench induced by the 2011 tohoku–oki earthquake. *Scientific Reports*, *3*(1). Retrieved from `http://dx.doi.org/ 10.1038/srep01915` doi: 10.1038/srep01915

Reynolds, R. W., Rayner, N. A., Smith, T. M., Stokes, D. C., & Wang, W. (2002, jul). An improved in situ and satellite sst analysis for climate. *Journal of Climate*, *15*(13), 1609–1625. Retrieved from `http://dx.doi.org/10.1175/1520-0442(2002) 015<1609:AIISAS>2.0.CO;2` doi: 10.1175/1520-0442(2002)015⟨1609:aiisas⟩2.0.co;2

Risien, C. M., & Chelton, D. B. (2008, nov). A global climatology of surface wind and wind stress fields from eight years of quikscat scatterometer data. *Journal of Physical Oceanography*, *38*(11), 2379–2413. Retrieved from `http://dx.doi.org/10.1175/2008JPO3881.1` doi: 10.1175/2008jpo3881.1

Sun, Y., Bakker, T., Ruf, C., & Pan, Y. (2023, feb). Effects of microplastics and surfactants on surface roughness of water waves. *Scientific Reports*, *13*(1). Retrieved from `http://dx.doi.org/10.1038/s41598-023-29088-9` doi: 10.1038/s41598-023-29088-9

Toole, J., Krishfield, R., Timmermans, M.-L., & Proshutinsky, A. (2011, sep). The ice-tethered profiler: Argo of the arctic. *Oceanography*, *24*(3), 126–135. Retrieved from `http://dx.doi.org/10.5670/oceanog.2011.64` doi: 10.5670/oceanog.2011.64

van Sebille, E., England, M. H., & Froyland, G. (2012, dec). Origin, dynamics and evolution of ocean garbage patches from observed surface drifters. *Environmental Research Letters*, *7*(4), 044040. Retrieved from `http://dx.doi.org/10.1088/1748-9326/7/4/044040` doi: 10.1088/1748-9326/7/4/044040

Yang, D., Chamecki, M., & Meneveau, C. (2014, mar). Inhibition of oil plume dilution in langmuir ocean circulation. *Geophysical Research Letters*, *41*(5), 1632–1638. Retrieved from `http://dx.doi.org/10.1002/2014GL059284` doi: 10.1002/2014gl059284

Appendix A Timescale to reach the terminal velocity

Consider a round particle moving at an instantaneous velocity w, subject to a buoyancy force $B = g(\rho_w - \rho_p)(4\pi/3)(d/2)^3$ and a drag force $D = (12/Re)(\rho_w w^2)\pi(d/2)^2$. Force balance acting on the particle leads to

$$\rho_p \frac{4\pi}{3}(\frac{d}{2})^3 \frac{dw}{dt} = g(\rho_w - \rho_p)\frac{4\pi}{3}(\frac{d}{2})^3 - \frac{12\mu w}{d}\pi(\frac{d}{2})^2. \tag{A1}$$

This forms an ODE for w

$$\frac{dw}{dt} = -\frac{18\mu}{\rho_p d^2} \times w + \frac{g(\rho_w - \rho_p)}{\rho_p}. \tag{A2}$$

Substituting equation (3) into (A2) gives

$$\frac{dw}{dt} = \frac{18\mu}{\rho_p d^2} \times (w - w_r). \tag{A3}$$

Let $\Delta w(t) = w(t) - w_r$, this yields a solution

$$\Delta w(t) = \Delta w(0) \times \exp\{-\frac{18\mu}{\rho_p d^2}t\}. \tag{A4}$$

That is, given any difference between the instantaneous velocity and the terminal velocity of a particle, the difference decreases exponentially in time. From the exponent in equation (A4), the e-folding timescale T_e for this velocity difference is

$$T_e = \frac{\rho_p d^2}{18\mu}. \tag{A5}$$

For $\rho_p \sim 1000 kg/m^3$ and $\mu = 0.001 Pa \cdot s$, equation (A5) gives $T_e = 0.05s$ even for large particles of diameter $d = 1mm$.

## Appendix B Graphical comparison with earlier studies

In this appendix we present comparison of our results in the idealistic cases to earlier relevant studies. Figure B1 shows a comparison of the result in our 2D idealistic case to that in Chenillat et al. (2021), Lebreton et al. (2012), Maximenko et al. (2012), and van Sebille et al. (2012). Figure B2 shows a comparison of the result in our neutrally buoyant case to that in Mountford and Morales Maqueda (2019) with the same color bar.
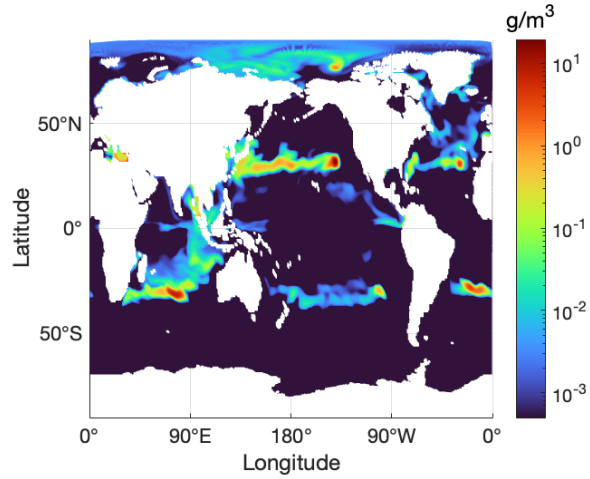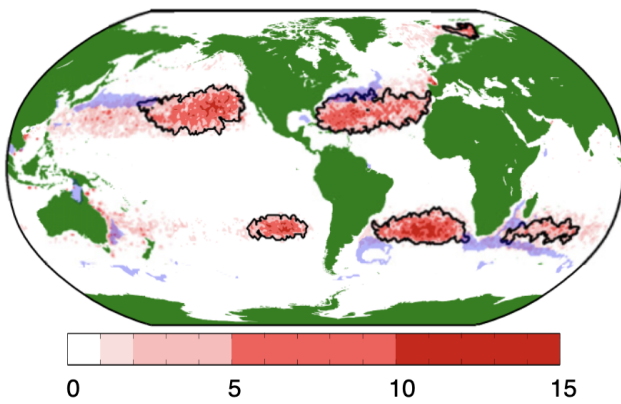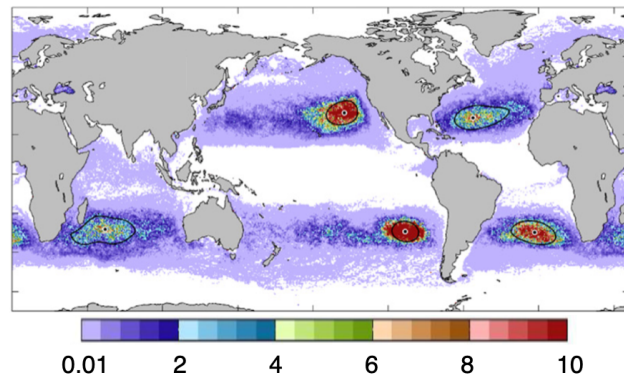
(a)
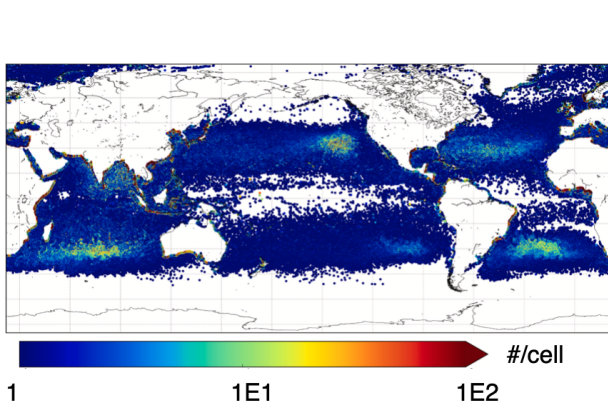
(b)
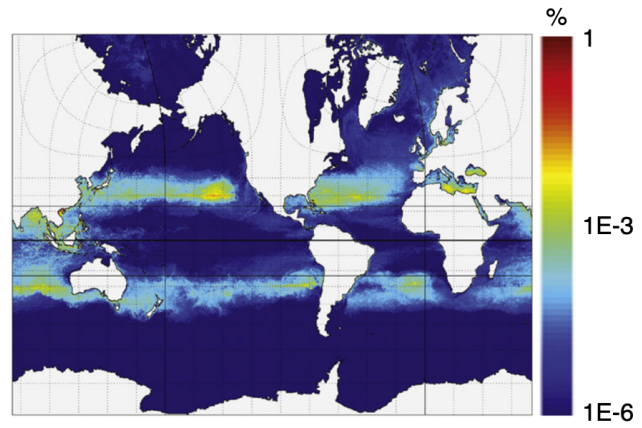
(c)

(d)

(e)

Figure B1: (a) copy of figure 2, (b) particle number density ($\#/[1/12° \times 1/12°]$ cell) taken from (Chenillat et al., 2021), (c) particle concentration (unit unspecified) taken from (Lebreton et al., 2012), (d) tracer amplification factor taken from (van Sebille et al., 2012), (e) particle concentration (unit unspecified) obtained by (Maximenko et al., 2012).
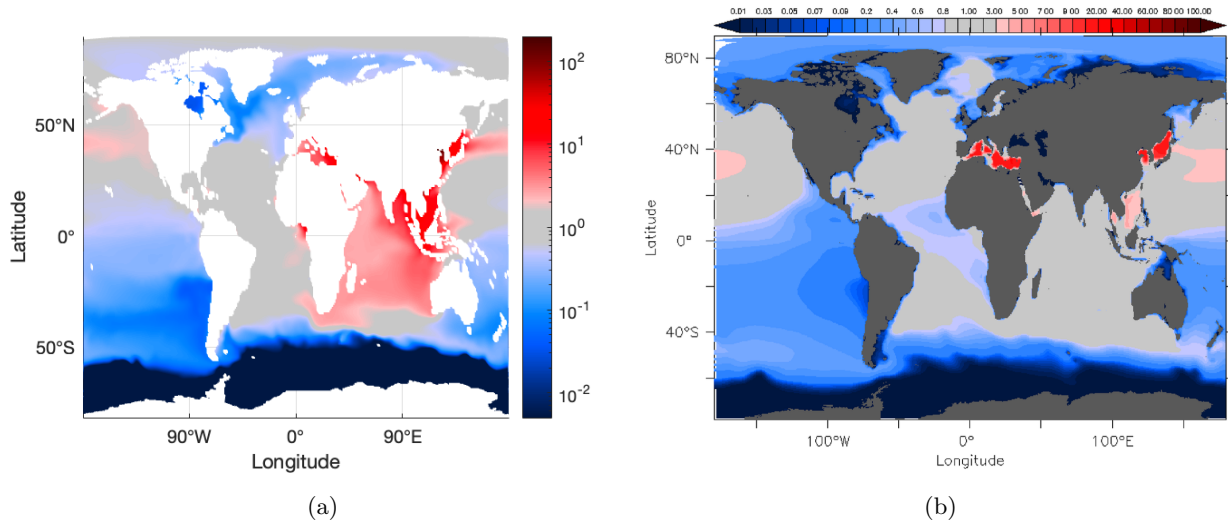
Figure B2: Neutrally buoyant particle surface distribution, normalized with global mean value, obtained by (a) our model and (b) (Mountford & Morales Maqueda, 2019) with the same color bar.